Nanoscale

Accepted Manuscript

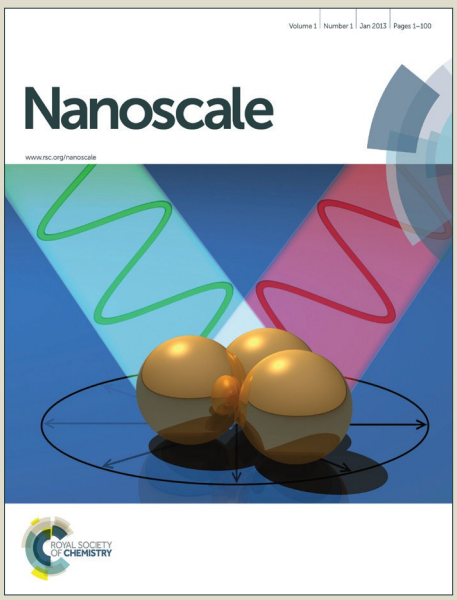

ROYAL SOCIETY OF CHEMISTRY

www.rsc.org/nanoscale

Nanoscale

ARTICLE

High performance, visible to mid-infrared photodetector based on graphene nanoribbons passivated by HfO_2

atrReceived 00th January 20xx,
Accepted 00th January 20xx

DOI: 10.1039/x0xx00000x

www.rsc.org/

Xuechao Yu,[a,†] Zhaogang Dong,[b,†] Yanping Liu,[a,†] Tao Liu,[a] Jin Tao,[a] Yongquan Zeng,[a] Joel K. W. Yang[c,b] and Qi Jie Wang[a,d,*]

Graphene has drawn tremendous attention as a promising candidate for electronic and optoelectronic applications owing to its extraordinary properties, such as broadband absorption and ultrahigh mobility. Nevertheless, the absence of bandgap makes graphene unfavorable for digital electronic or photonic applications. Although patterning graphene into nanostructures with quantum confinement effect is able to open a bandgap, devices based on these graphene nanostructures generally suffer from the low carrier mobility and scattering losses. In this paper, we demonstrated that encapsulation of atomic layer deposited high-quality HfO_2 film will greatly enhance the carrier mobility and decrease the scattering losses of graphene nanoribbon, because this high-*k* dielectric layer weakens carrier Coulombic interactions. In addition, photodetector based on HfO_2 layer capped graphene nanoribbons can cover a broadband wavelength from visible to mid-infrared at room temperature, exhibiting ~10 times higher responsivity than the one without HfO_2 layer in visible regime and ~8 times higher in mid-infrared regime. The method employed here could be potentially used as a general approach to improve the performance of graphene nanostructures for electronic and optoelectronic applications.

Introduction

Graphene, a two-dimensional allotrope of honeycomb carbon atoms, has been considered as an attractive building block for electronic and optoelectronic applications,[1-6] such as novel photodetectors with ultrafast speed[7-9] and broadband operation wavelength ranging from visible to Terahertz.[10-12] Such broadband absorption is emerged from the unique conic band structure and linear energy dispersion of massless Dirac fermions.[13-15] Nevertheless, this zero bandgap characteristic of the monolayer graphene introduces some limitations that render its applications. First, the low absorption (~2.3%) of monolayer graphene via interband transitions is still a critical challenge.[16] Second, the zero bandgap leads to a short photogenerated carrier lifetime in the picosecond level, which causes fast electron-hole recombinations.[17, 18] As a result, the photoresponse of the pristine graphene photodetectors is quite weak nowadays.

Several approaches have been used to enhance the photoresponse of graphene photodetectors. For example, graphene quantum dots (QGDs) arrays were successfully employed to create a bandgap of around 100 meV to improve the responsivity of pure graphene photodetectors through bandgap and defect engineering.[19] Although a broadband photodetector with a responsivity of up to 8.6 AW^{-1} was achieved in the visible range, it still remains as a challenge to obtain room temperature operation of graphene photodetectors with a relatively fast response speed in a broadband range due to the random scattering losses. Alternatively, graphene nanoribbons (GNRs)[20-22] have been demonstrated to have a bandgap opening by utilizing the quantum confinement effect,[23-25] which has been realized through unzipping of carbon nanotube,[26] lithographic patterning[23-25] and other chemical approaches.[27, 28] However, disordered edges, impurities and phonon scattering of the GNR reduce the carrier mobility and increase the carrier scattering losses, which limit the device performances.[29] Previously, graphene photodetectors based on ~240-nm-wide GNRs were reported with a low photoresponse in the mid-infrared regime, because graphene nanoribbon with this width cannot open a sufficient bandgap, even though the light-graphene interaction is enhanced by graphene plasmons.[30] On the contrary, ultra-narrow GNRs with widths of ~2-5 nm was used for graphene photodetector for achieving a considerable bandgap.[26] However, the performance of the device are significantly limited by the low mobility of GNR as induced by the tremendous carrier scattering losses from defects and GNR edges with such a narrow width. Therefore, it is critical to design appropriate GNR structures to obtain a suitable

[a] Centre for OptoElectronics and Biophotonics, School of Electrical and Electronic Engineering, Nanyang Technological University, 639798, Singapore.
[b] Institute of Materials Research and Engineering, Agency for Science, Technology and Research (A*STAR), 2 Fusionopolis Way, #08-03 Innovis, 138634, Singapore.
[c] Singapore University of Technology and Design, 8 Somapah Road, 487372, Singapore.
[d] Centre for Disruptive Photonics Technologies, Nanyang Technological University, 21 Nanyang Link, 637371, Singapore.
†Equal contribution.
*Corresponding email: qjwang@ntu.edu.sg
Electronic Supplementary Information (ESI) available: Method, characterization results, calculation of photoresponsivity, calculation of photoconductive gain. See DOI: 10.1039/x0xx00000x

bandgap for broadband operation, while still maintaining its high mobility in order to achieve high photodetection performances.

In this paper, we demonstrated a graphene field-effect transistor (FET) made of 10-nm-wide GNRs encapsulated by an ultrathin high-*k* HfO_2 layer, where the obtained GNR FET shows a semiconductor behaviour with an ON/OFF ratio of 7±1. The GNR photodetector shows a high responsivity across a broadband wavelength range from visible to mid-infrared, *i.e.* 1.75 AW^{-1} in the visible, 1.5 AW^{-1} in the near-infrared and 0.18 AW^{-1} in the mid-infrared, at room temperature with a source-drain voltage as low as 10 mV. In addition, the photoresponse speed of our GNR photodetector, fabricated by electron-beam lithography (EBL) and reactive-ion etching (RIE), is relatively faster than those devices obtained by chemical methods.[19, 22, 31] These promising performance is due to the proper designs of GNR width for broadband operation, and the increment of carrier mobility due to the reduction of carrier scattering losses in GNR via high-*k* HfO_2 passivation.[32-34] Our work reveals the importance of dielectric environment for graphene nanostructures and it provides insights to optimize the graphene-based photodetectors and transistors for optoelectronic and electronic applications.

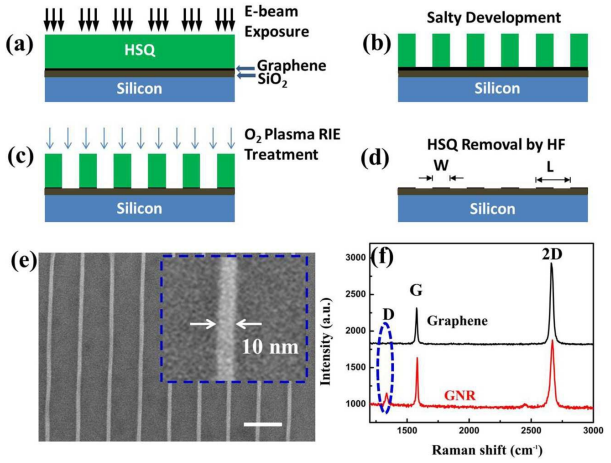

Fig. 1 Electron beam lithography (EBL) processes and characterization of graphene nanoribbon (GNR). (a)-(d) Schematic illustration on the process to fabricate GNR using EBL and reactive-ion etching (RIE) oxygen plasma treatment. (e) Scanning electron micrograph (SEM) image of the hydrogen silsesquioxane (HSQ) resist mask prior to the RIE oxygen plasma treatment. The scale bar is 100 nm. The inset presents a close-up SEM image of the 10-nm-wide HSQ resist mask. (f) Raman spectra of the exfoliated monolayer graphene and GNR.

Results and discussion

Monolayer graphene was fabricated by mechanical exfoliation of highly-ordered pyrolytic graphite (HOPG) on SiO_2/Si wafer and identified by optical microscope and Raman spectroscopy.[35] We first fabricated the graphene FET devices using standard photolithography, followed by an e-beam evaporation of Ti/Au electrodes (20 nm/80 nm). The fabrication processes of GNR FET devices are shown in Fig. 1(a)-(d), where a monolayer graphene was patterned into nanoribbons by using electron beam lithography (EBL) and reactive-ion etching (RIE) oxygen plasma treatment. First, a negative e-beam resist, hydrogen silsesquioxane (HSQ), with a thickness of ~30 nm was spin-coated onto the substrate. After the electron-beam exposure, the sample was then developed by NaOH/NaCl salty solution,[36] where the corresponding scanning electron micrograph (SEM) image of the 10-nm-wide HSQ resist mask is shown in Fig. 1(e). Here, we did not take SEM images of GNR directly because the high energy electron beams will change the doping level of graphene so as to affect GNR photodetector's performance, where this doping effect has been reported previously.[37-40] With this HSQ etching mask, patterns were transferred onto the underlying graphene monolayer via RIE oxygen plasma treatment. HSQ was then removed by immersing the sample in hydrofluoric acid solution (HF ~2%) for 30 seconds. Furthermore, Raman spectrum of GNR presents a clear D-peak at ~1350 cm^{-1} in Fig. 1(f), indicating that the EBL process induced defects, impurities and edge scatterings in the GNR.

The field-effect transistor (FET) devices were fabricated for both unpatterned graphene and 10-nm-wide GNRs. V_{DS}, I_{DS} and V_G denote the source-drain bias voltage, current, and bottom gate voltage. The devices have a pair of metal pad (Ti/Au) as source/drain metal contacts, a heavily p-doped Si as backgate, and 285-nm-thick SiO_2 as gate dielectric. Moreover, Fig. S2 and Fig. 2 show the comparison of electrical characterization of the unpatterned graphene and GNR-based FETs at room temperature, where both measured I_{DS}-V_{DS} curves in Fig. S2(a) and Fig. 2(a) are linear over a wide range of gate voltages. Such linear dependence indicates that the Ti/Au electrodes have a good Ohmic contact. By comparing Fig. S2(b) and Fig. 2(b), GNR-based FET exhibits a semiconducting transport behaviour with an ON/OFF ratio of ~7±1, where the ON/OFF ratio was measured at V_G–V_D = −80 V, and V_D denotes the neutral point.

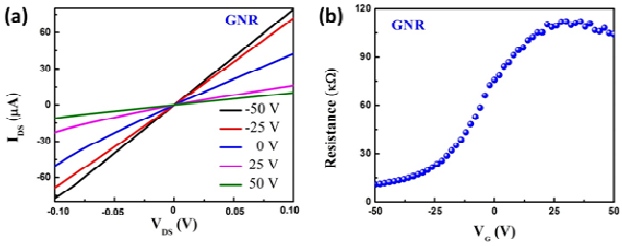

Fig. 2 Electrical characterizations of GNR-based field-effect transistor (FET) at room temperature. (a) I_{DS}-V_{DS} curves recorded at different gate voltages. (b) Dependence of the resistance on gate voltage recorded at V_{DS}=10 mV, indicating a semiconducting behaviour curve.

The GNR FET is shown to behave like a semiconducting material with an adequate bandgap to operate in the mid-infrared regime at room temperature, and the relationship between the GNR width and its bandgap can be expressed as:[24]

$$E_g(W) \approx \frac{e^2}{W} e^{-W/W_0}, \quad (1)$$

where W_0 indicates the renormalization of geometrical charging energy by virtual charge fluctuations and it has a typical value of ~40 nm.[24] e is the electron charge and W is the actual width of GNR. For instance, the 10-nm-wide GNR possesses a bandgap of ~100 meV for our obtained samples.

On the other hand, the mobility of GNR device is reduced significantly as compared to the unpatterned graphene devices, and the carrier mobility μ can be calculated by:

$$\mu = \frac{Ld}{M\varepsilon_0\varepsilon_r} \times \frac{dI_{DS}}{dV_G} \times \frac{1}{V_{DS}}, \quad (2)$$

where L, M denote the channel length, and total width of the FET respectively. d denotes the thickness of SiO_2 layer (285 nm in our devices). One should note that the actually width of GNR FET with graphene nanoribbons is M/10 according to the ribbon ratio (*i.e.* 10%) as shown in Fig. 1(e). ε_0 and ε_r represent the dielectric constant of vacuum and SiO_2 (ε_r=3.9), respectively. Based on Eq. (2), the mobility of GNR FET is ~100 $cm^2V^{-1}s^{-1}$, which is ~25 times smaller than the pristine graphene FETs fabricated in our experiment. The relatively low mobility of GNR is caused by carrier scattering with impurities, defects, and surface roughness.[41] Although a built-in electrical field can be used to separate photo-excited carriers in optoelectronic devices,[31] the low mobility (~100 $cm^2V^{-1}s^{-1}$) restrains its potential applications.

The carrier mobility could be enhanced by passivating a layer of high-k dielectric material, such as HfO_2, on top of GNR, where the detailed sample schematic structure is shown in Fig. 3(a), and this approach of using high-k dielectrics was previously employed in MoS_2[31, 32] and graphene devices.[33, 34] The source and drain electrodes are exposed by selectively etching with HF solution after the photolithography process. The use of this high-k dielectric material (HfO_2) is that it can change the dielectric environment of GNR so as to reduce the carrier scattering from impurities, defects, and surface roughness through dielectric screening. The HfO_2 layer is grown by using atomic layer deposition (ALD) method, where atomic force microscope (AFM) was then used to characterize the surface profile of the ALD grown HfO_2 film, and the line-scan profile shows a thickness of 1.8 nm in Fig. 3(a) for 20 ALD process cycles. The thickness of the HfO_2 film can be well controlled based on the number of ALD process cycles. Moreover, the high crystallization quality of HfO_2 layer was confirmed by the X-ray photoelectron spectroscopy (XPS) measurements in Fig. S1.

The electrical transport characterizations were then carried out for both the GNR-based FETs with and without HfO_2 film under the same conditions. The I_{DS}-V_{DS} curves, as shown in Fig. 3(b), are linear and symmetric at the small bias voltages. All devices with deposited HfO_2 show a larger source-drain current than the one without HfO_2, which is because of the mobility enhancement of GNR due to dielectric screening. In order to demonstrate the mechanism of dielectric environment effect on carrier scattering as caused by the charged impurity, we compared the results on mobility by using two kinds of dielectric materials capped on GNR as shown in Fig. 3(e). For the first scenario, the capping material has a higher dielectric constant than GNR, *i.e.* $\varepsilon_e > \varepsilon_g$. ε_e refers to the dielectric constant of HfO_2 in our case and ε_g refers to the dielectric constant of graphene. For the second scenario, the capping material is a low-k materials with $\varepsilon_e < \varepsilon_g$, *e.g.* ε_e = 1. Due to the mismatch of dielectric constant between GNR and the capping material, image charges are induced in the capping dielectric materials.[32] To be more specific, the induced array of image charges are located at $z_n=na$, where a is the thickness of GNR and n=±1, ±2, … The n-th point charge has a magnitude of $e\gamma^{|n|}$ and $\gamma=(\varepsilon_e-\varepsilon_g)/(\varepsilon_e+\varepsilon_g)$. Then, we could calculate the net electric potential seen by the electron due to these image charges as:[42]

$$V_{coub}(\rho,z) = \sum \frac{e\gamma^{|n|}}{4\pi\varepsilon_0\varepsilon_s\sqrt{\rho^2+(z-z_n)^2}} z, \quad (3)$$

where ε_0 is the vacuum permittivity.

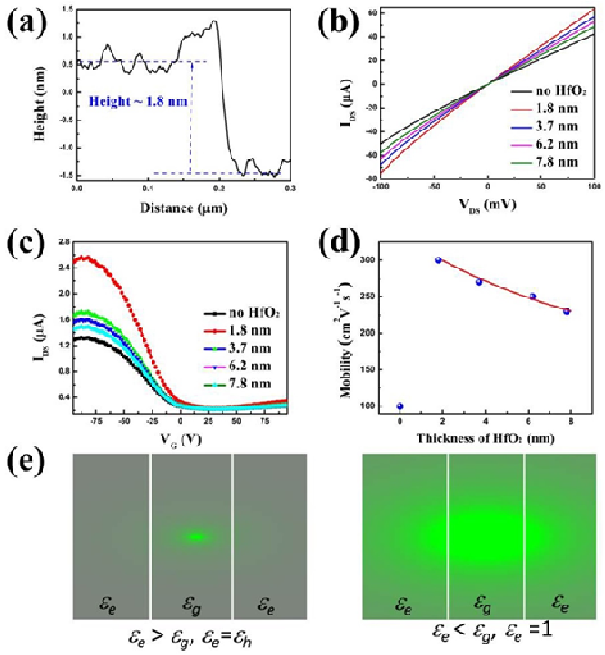

Fig. 3 Schematic and characterization results of GNR-based FET deposited with HfO_2 films. (a) Height profile of the HfO_2 film as measured by atomic force microscope (AFM). The HfO_2 film was grown using atomic layer deposition (ALD) method with 20 cycles. (b) I_{DS}-V_{DS} curves of different HfO_2 coated GNR-based FET recorded at V_{DS}=10 mV. (c) I_{DS}-V_G curves of HfO_2 coated GNR arrays based FET recorded at V_{DS}=10 mV. (d) Mobility of GNR-based FET with a different thickness of HfO_2 layer. (e) Coulomb potential corresponding to two different dielectric environments, i.e. $\varepsilon_g>\varepsilon_e$ and $\varepsilon_g<\varepsilon_e$. ε_h denotes the dielectric constant of HfO_2.

Figure 3(e) shows the Coulomb potential contours, from which we can conclude that the Coulomb potential is enhanced for low-k case, while it is strongly damped for the high-k case. In addition, the GNR FET with the 1.8-nm-thick HfO_2 layer shows a larger mobility value, where the mobility decreases with the increment of HfO_2 layer thickness as shown

in Fig. 3(d). This phenomenon is consistent with Eq. (3) and it can be explained by the increment of defects and surface roughness induced scattering with thicker ALD HfO_2 layers.[42] Here, we would like to mention that we could not carry out experiments with the thickness of the HfO_2 layer being below 1.8 nm since the ALD fabricated film is not uniform with less than 20 ALD cycles. Further improvements are also possible if using other materials with thinner layer and better uniformity, such as ALD grown Al_2O_3[43, 44] or monolayer h-BN.[45]

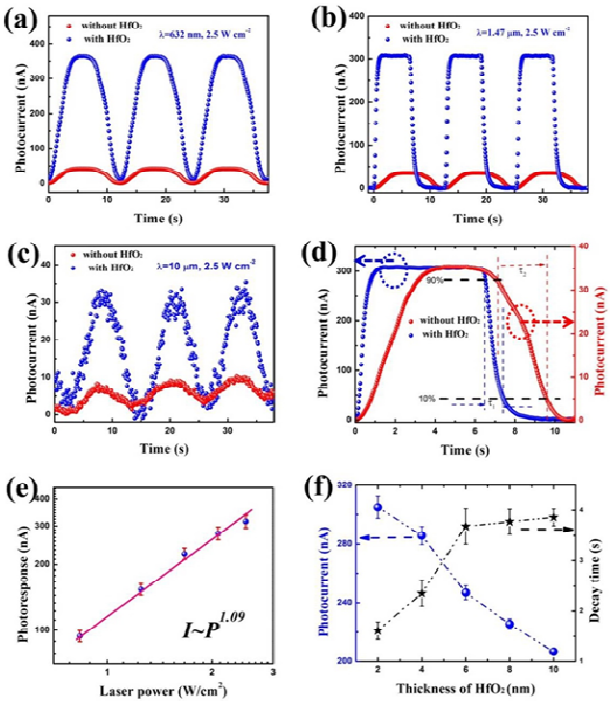

Fig. 4 (a) Photodetection measurement of HfO_2 capped GNR-based FETs with visible, near-infrared and mid-infrared lasers. (a)-(c) Time-dependent photocurrent measurements on the GNR-based FETs under the laser illumination with the wavelength of 632 nm, 1.47 μm, and 10 μm, respectively. The power density for all the measurements was kept at 2.5 Wcm^{-2}. (d) Photocurrent of 1.8-nm-thick HfO_2 capped GNR FETs measured in one period of modulation with the 1.47 μm laser illumination (12 mW). (e) Power dependence of the photocurrent with 1.47 μm lasers, for every laser illumination we measured 3 different samples. (f) Photocurrent and decay time measurements of graphene with different thicknesses of HfO_2 film, corresponding to thicknesses as shown in Fig. 3(e), at least 3 different samples are measured with the same thickness of HfO_2 film.

We measured the optoelectronic properties of bare and HfO_2 capped GNR photodetectors and their time-dependent photoresponse, with the excitation laser wavelengths of 632 nm, 1.47 μm and 10 μm, respectively. A parabolic mirror with a micromechanical stage was used to focus laser spot onto the sample and the estimated power intensity is ~2.5 Wcm^{-2}. The time-dependent photocurrent responses at different wavelengths are shown in Fig. 4(a)-(c). It is shown that, in a broadband range from visible, to near-infrared, and mid-infrared, the photocurrent of HfO_2 capped GNR photodetectors is about ~8-10 times higher than the one without HfO_2 capping, corresponding to a responsivity of 1.75 AW^{-1}, 1.5 AW^{-1}, 0.18 AW^{-1}, respectively, with a small source-drain bias voltage of only 10 mV. This high responsivity achieved in our devices can be attributed to the enhancement of mobility through dielectric screening. The response time is still in the second level as shown in Fig. 4(a)-(d), which is limited by the long trapping lifetime of carriers in the defect and edges states. However, the response speed demonstrated here is about one order of magnitude faster than the previous reports on randomly distributed graphene quantum dot (GQD) photodetector[19] which has complex deep surface and edge states and an electron trapping time of ~30 seconds. The improvement was achieved by e-beam lithography fabrication method which is used to define the edge and surface states of graphene nanoribbons with low-level chemical processes involved, thus producing graphene nanoribbons with cleaner and less surface and edge defects. The usage of high-*k* HfO_2 as a passivated layer, apart from enhancing the carrier mobility, can also efficiently modify the edge and defect states of GNRs, leading to a faster response speed. Moreover, further improvements of the response speed are possible by using monolayer h-BN for dielectric engineering or optimizing nanofabrication process to achieve well-defined edges and clean surfaces with less defects and residues.

Figure 4(e) presents the detailed photoresponse as a function of the laser power at the wavelength of 1.47 μm, and it is fitted by the relation $I_{PC} = CP^{\gamma}$, where C is a constant and P is the illumination power. The value of γ is calculated to be ~1.09 and this relative high value of γ in GNR is contributed to the 1-*d* transport characteristic of GNR and relatively high mobility of our HfO_2 capped GNR devices. Further increment of the HfO_2 thickness will increase the response time slightly as shown in Fig. 4(f), which is due to the increased density of defect states and trapping states with increasing thickness of the dielectric layer.[42] We note that the HfO_2 capped GNR photodetector operated in the mid-infrared exhibit a longer photoresponse time as compared to those in the visible and near-infrared regimes as shown in Fig. 4(a)-(c), where the detailed mechanism for this slower decay time at mid-infrared regime need further investigations.

The photocurrent obtained in our HfO_2 capped graphene nanoribbons is higher than that of bare graphene nanoribbons[31] and chemically etched GQDs,[19] because the Coulomb interactions and carrier/defects scatterings are strongly decreased through the passivation of a high-*k* dielectric layer and e-beam lithography fabrication of the GNRs. The design of a proper width of graphene nanoribbon is important for optoelectronic applications. For example, we measured the photodetector with 100-nm-wide GNR, in which the photoresponse is only ~5 mAW^{-1} under illumination with a 10 μm laser as shown in Fig. S3. On the other hand, the photoresponse in our work is higher than the one of using ~240-nm-wide graphene nanoribbons, because the GNR width is not narrow enough to open a bandgap according to Eq. (1), even though the absorption is enhanced by graphene plasmons.[30] In comparison, although the ultra-narrow (<5 nm)

GNR was fabricated by unzipping of carbon nanotube (CNT) exhibiting typical semiconductor behaviour,[26] the photoresponse is very weak due to the strong edge scattering losses, which increase as W^{-4} with W being the width of the nanoribbons.[41] Furthermore, other newly proposed 2D materials with narrow bandgaps[46] combined with this dielectric engineering strategy are promising to develop novel mid-infrared photodetector.

Conclusions

In summary, we demonstrate a novel strategy to enhance the mobility of 10-nm-wide GNR FETs by capping a high-*k* dielectric HfO_2 layer, which improves the mobility of the GNR FETs by ~3 times, as compared to the pure GNR devices. Such an improvement in mobility is attributed to the reduced carrier scatterings in capped GNR. Furthermore, the optical characterization results of HfO_2 capped GNR photodetectors show that the response time will be ~5 times faster and the responsivity was enhanced by ~10 times in the visible and near-infrared, and ~8 times in the mid-infrared. We believe that our work paves a way towards high performance and flexible graphene-based optoelectronic devices, especially with the potential combination of large-area CVD growth of graphene and the CMOS technology.[47]

Acknowledgements

This work is supported by (MOE2011-T2-2-147 and MOE2011-T3-1-005) from Ministry of Education, Singapore. Z. D. and J. K. W. Y. would like to acknowledge the funding support from the Agency for Science, Technology and Research (A*STAR) Young Investigatorship (grant number 0926030138), SERC (grant number 092154099), and National Research Foundation (grant number NRF-CRP 8-2011-07). X. Y., Z. D. and Y. L. contribute equally to this work.

Notes and references

1. A. K. Geim and K. S. Novoselov, *Nat. Mater.*, 2007, **6**, 183-191.
2. K. S. Novoselov, V. I. Falko, L. Colombo, P. R. Gellert, M. G. Schwab and K. Kim, *Nature*, 2012, **490**, 192-200.
3. F. H. L. Koppens, T. Mueller, P. Avouris, A. C. Ferrari, M. S. Vitiello and M. Polini, *Nat. Nano.*, 2014, **9**, 780-793.
4. L. Shao, X. Wang, H. Xu, J. Wang, J.-B. Xu, L.-M. Peng and H.-Q. Lin, *Adv. Opt. Mater.*, 2014, **2**, 162-170.
5. B. J. Schultz, R. V. Dennis, V. Lee and S. Banerjee, *Nanoscale*, 2014, **6**, 3444-3466.
6. W. Jie and J. Hao, *Nanoscale*, 2014, **6**, 6346-6362.
7. K. J. Tielrooij, PiatkowskiL, MassicotteM, WoessnerA, MaQ, LeeY, K. S. Myhro, C. N. Lau, P. Jarillo Herrero, N. F. van Hulst and F. H. L. Koppens, *Nat. Nano.*, 2015, **10**, 437-443.
8. T. Mueller, F. Xia and P. Avouris, *Nat. Photon.*, 2010, **4**, 297-301.
9. T. J. Echtermeyer, P. S. Nene, M. Trushin, R. V. Gorbachev, A. L. Eiden, S. Milana, Z. Sun, J. Schliemann, E. Lidorikis, K. S. Novoselov and A. C. Ferrari, *Nano Lett.*, 2014, **14**, 3733-3742.
10. Q. Bao and K. P. Loh, *ACS Nano*, 2012, **6**, 3677-3694.
11. Z. Sun and H. Chang, *ACS Nano*, 2014, **8**, 4133-4256.
12. X. Cai, A. B. Sushkov, R. J. Suess, M. M. Jadidi, G. S. Jenkins, L. O. Nyakiti, R. L. Myers-Ward, S. Li, J. Yan, D. K. Gaskill, T. E. Murphy, H. D. Drew and M. S. Fuhrer, *Nat. Nano.*, 2014, **9**, 814-819.
13. K. S. Novoselov, A. K. Geim, S. V. Morozov, D. Jiang, M. I. Katsnelson, I. V. Grigorieva, S. V. Dubonos and A. A. Firsov, *Nature*, 2005, **438**, 197-200.
14. A. H. Castro Neto, F. Guinea, N. M. R. Peres, K. S. Novoselov and A. K. Geim, *Rev. Mod. Phys.*, 2009, **81**, 109-162.
15. J. Li, L. Niu, Z. Zheng and F. Yan, *Adv. Mater.*, 2014, **26**, 5239-5273.
16. R. R. Nair, P. Blake, A. N. Grigorenko, K. S. Novoselov, T. J. Booth, T. Stauber, N. M. R. Peres and A. K. Geim, *Science*, 2008, **320**, 1308-1308.
17. P. A. George, J. Strait, J. Dawlaty, S. Shivaraman, M. Chandrashekhar, F. Rana and M. G. Spencer, *Nano Lett.*, 2008, **8**, 4248-4251.
18. K. J. Tielrooij, J. C. W. Song, S. A. Jensen, A. Centeno, A. Pesquera, A. Zurutuza Elorza, M. Bonn, L. S. Levitov and F. H. L. Koppens, *Nat. Phys.*, 2013, **9**, 248-252.
19. Y. Zhang, T. Liu, B. Meng, X. Li, G. Liang, X. Hu and Q. J. Wang, *Nat. Commun.*, 2013, **4**, 1811.
20. Y. F. Zhu, Q. Q. Dai, M. Zhao and Q. Jiang, *Sci. Rep.*, 2013, **3**, 1524.
21. V. Barone, O. Hod and G. E. Scuseria, *Nano Lett.*, 2006, **6**, 2748-2754.
22. B. Chitara, L. S. Panchakarla, S. B. Krupanidhi and C. N. R. Rao, *Adv. Mater.*, 2011, **23**, 5419-5424.
23. M. Y. Han, B. Özyilmaz, Y. Zhang and P. Kim, *Phys. Rev. Lett.*, 2007, **98**, 206805.
24. F. Sols, F. Guinea and A. H. C. Neto, *Phys. Rev. Lett.*, 2007, **99**, 166803.
25. X. Liang, Y.-S. Jung, S. Wu, A. Ismach, D. L. Olynick, S. Cabrini and J. Bokor, *Nano Lett.*, 2010, **10**, 2454-2460.
26. D. Wei, L. Xie, K. K. Lee, Z. Hu, S. Tan, W. Chen, C. H. Sow, K. Chen, Y. Liu and A. T. S. Wee, *Nat. Commun.*, 2013, **4**, 1374.
27. X. Li, X. Wang, L. Zhang, S. Lee and H. Dai, *Science*, 2008, **319**, 1229-1232.
28. A. N. Abbas, G. Liu, A. Narita, M. Orosco, X. Feng, K. Müllen and C. Zhou, *J. Am. Chem. Soc.*, 2014, **136**, 7555-7558.
29. E. Ulrich Stützel, T. Dufaux, A. Sagar, S. Rauschenbach, K. Balasubramanian, M. Burghard and K. Kern, *Appl. Phys. Lett.*, 2013, **102**, 043106.
30. M. Freitag, T. Low, W. Zhu, H. Yan, F. Xia and P. Avouris, *Nat. Commun.*, 2013, **4**, 1951.
31. J. G. Son, M. Son, K.-J. Moon, B. H. Lee, J.-M. Myoung, M. S. Strano, M.-H. Ham and C. A. Ross, *Adv. Mater.*, 2013, **25**, 4723-4728.
32. Z.-Y. Ong and M. V. Fischetti, *Phys. Rev. B*, 2013, **88**, 165316.
33. L. Liao, J. Bai, R. Cheng, Y.-C. Lin, S. Jiang, Y. Huang and X. Duan, *Nano Lett.*, 2010, **10**, 1917-1921.
34. F. Chen, J. Xia, D. K. Ferry and N. Tao, *Nano Lett.*, 2009, **9**, 2571-2574.
35. X. Yu, J. Tao, Y. Shen, G. Liang, T. Liu, Y. Zhang and Q. J. Wang, *Nanoscale*, 2014, **6**, 9925-9929.
36. Z. Dong, M. Asbahi, J. Lin, D. Zhu, Y. M. Wang, K. Hippalgaonkar, H.-S. Chu, W. P. Goh, F. Wang, Z. Huang and J. K. W. Yang, *Nano Lett.*, 2015, **15**, 5976-5981.
37. I. Childres, L. A. Jauregui, M. Foxe, J. Tian, R. Jalilian, I. Jovanovic and Y. P. Chen, *Appl. Phys. Lett.*, 2010, **97**, 173109.
38. D. Teweldebrhan and A. A. Balandin, *Appl. Phys. Lett.*, 2009, **94**, 013101.

39. M. M. Ugeda, I. Brihuega, F. Hiebel, P. Mallet, J.-Y. Veuillen, J. M. Gómez-Rodríguez and F. Ynduráin, *Phys. Rev. B*, 2012, **85**, 121402.
40. L. Tao, C. Qiu, F. Yu, H. Yang, M. Chen, G. Wang and L. Sun, *J. Phys. Chem. C*, 2013, **117**, 10079-10085.
41. T. Fang, A. Konar, H. Xing and D. Jena, *Phys. Rev. B*, 2008, **78**, 205403.
42. D. Jena and A. Konar, *Phys. Rev. Lett.*, 2007, **98**, 136805.
43. C. Goo Kang, S. Kyung Lee, T. Jin Yoo, W. Park, U. Jung, J. Ahn and B. Hun Lee, *Appl. Phys. Lett.*, 2014, **104**, 161902.
44. C. G. Kang, S. K. Lee, S. Choe, Y. G. Lee, C.-L. Lee and B. H. Lee, *Opt. Express*, 2013, **21**, 23391-23400.
45. H. Zeng, C. Zhi, Z. Zhang, X. Wei, X. Wang, W. Guo, Y. Bando and D. Golberg, *Nano Lett.*, 2010, **10**, 5049-5055.
46. S. Zhang, Z. Yan, Y. Li, Z. Chen and H. Zeng, *Angew. Chem. Int. Ed.*, 2015, **54**, 3112-3115.
47. X. Zhang, J. Ning, X. Li, B. Wang, L. Hao, M. Liang, M. Jin and L. Zhi, *Nanoscale*, 2013, **5**, 8363-8366.